Butcher & Oemler Cluster A2111:
A Head-on Merger at $z = 0.23$

Q. Daniel Wang and Melville Ulmer

Dearborn Observatory, Northwestern University

2131 Sheridan Road, Evanston, IL 60208-2900

E-mail: wqd@nwu.edu and ulmer@ossenu.astro.nwu.edu

and

Russell J. Lavery

Department of Physics & Astronomy, Iowa State University

1 Osborn Drive, Ames, IA 50011-3160

E-mail: lavery@iastate.edu

ABSTRACT

We present *ROSAT* PSPC and HRI observations of A2111, the richest galaxy cluster photometrically surveyed by Butcher & Oemler (1984). The cluster contains a distinct comet-shaped X-ray subcomponent, which appears hotter than the rest of the cluster. The galaxy and X-ray surface brightness distributions of the cluster show a similarly elongated morphology. These results suggest that the cluster is undergoing a head-on subcluster merger. This merger may also be responsible for the high fraction of gas-rich blue galaxies observed in the cluster. We have further detected a poor cluster along the merging axis and at a projected distance of ~ 5 Mpc from A2111.

Subject headings: cosmology: observations — large-scale structure of universe — galaxies: clusters: individual (A2111) — galaxies: evolution — X-rays: general

1. Introduction

It is becoming increasingly clear that clusters of galaxies are evolving even at relatively recent epochs. Analysis of galaxy and X-ray surface brightness distributions (e.g., Geller & Beers 1982; Dressler & Shectman 1988; Jones & Forman 1992) indicate that about 40% of nearby clusters contain substructure. In particular, recent X-ray observations have revealed that A2256 and A754, two nearby rich clusters, are apparently undergoing major mergers with subclusters (Briel et al. 1991; Briel & Henry 1994; Henry & Briel 1995; Henriksen & Markevitch 1996). Therefore, at least some of the clusters are dynamically young system. Furthermore, it has been known for a long time that the average proportion of blue galaxies observed in rich clusters at $z \gtrsim 0.2$ is considerably higher than at lower redshifts (Butcher & Oemler 1984 — BO hereafter; Lavery &

Henry 1986; Newberry et al. 1988; Dressler & Gunn 1992; Fabricant, Bautz, & McClintock 1994). Yet unknown, however, is whether or not there is a connection between the dynamic state and the blue galaxy population of a cluster (e.g., Couch et al. 1994; Zabludoff et al. 1996; Tomita et al 1996).

The rich cluster A2111 provides an ideal site to explore this connection. The cluster is one of the richest clusters in the Universe. Among 33 rich clusters studied by BO (also see Butcher, Oemler, & Wells 1983, BOW hereafter), A2111 has the highest total number of cluster members brighter than $M_v = -20$ ($N_{30\%} = 155$). It also contains a large fraction of blue galaxies ($f_b = 0.16 \pm 0.03$; BO; Lavery & Henry 1986), higher than the average of clusters at similar redshifts ($z = 0.2 - 0.3$), let alone that of nearby ones ($f_b \lesssim 0.05$). At its redshift of 0.228, A2111 permits a detailed study of both the X-ray-emitting intracluster medium (ICM) and the cluster galaxy population.

Based on two *ROSAT* observations and a deep R-band CCD image, we find that A2111 is most likely undergoing a head-on subcluster collision, and we argue that the collision may be responsible for the observed blue galaxy population. In the following, we first briefly describe the observations and the data reduction (§2), and then present our results from a detailed analysis of the data, including a study of the galaxy distribution (§3). We explore the implications of our results on both the dynamic state and the galaxy population of the cluster (§4). Finally in §5, we summarize our results and conclusions. To be consistent with previous studies (e.g., BO), we adopt $H_o = 50h_{50}$ km s^{-1} Mpc^{-1} and $q_o = 0.1$ throughout the paper. Thus, $1' = 0.29h_{50}^{-1}$ Mpc at the redshift of A2111.

2. Observations and Data Reduction

Our X-ray observations utilized the two X-ray detectors aboard *ROSAT* (Trümper 1992 and references therein): the Position Sensitive Proportional Counter (PSPC; Obs. No. rp800479) and the High Resolution Imager (RHRI; rh800666). The total exposures are 7,511 s (PSPC) and 62,287 s (RHRI). Briefly, the PSPC has a point response function (PSF) of $\sim 0\rlap{.}'5$ FWHM within the central $10'$ radius and has about seven independent energy bands in the 0.1-2.4 keV range. The total field of view of the PSPC observation is $2°$ diameter. But we use only the data within the central $16'$ radius to avoid complications caused by both the detector's window supporting structure and the badly degraded PSF outside this radius (Hasinger et al. 1992; Nichol et al. 1994). The RHRI observation has a higher spatial resolution of $\sim 5''$ on-axis. However, the quantum efficiency of the RHRI is about a factor of 3 lower than that of the PSPC, and the non-cosmic X-ray background is much higher (by a factor of ~ 10). Thus, the RHRI observation is useful primarily for resolving source confusion and bright emission peaks.

In our study of the diffuse cluster emission, we excise point-like X-ray sources, detected with signal-to-noise ratios greater than 3, by excluding data within 90% source flux-encircled

radii. Compared to A2111, all the X-ray sources in the vicinity (Figs. 1-2) are relatively faint. In particular, within a $3.'5$ radius of the cluster, we find no significant point-like emission. After rotating the RHRI image by an angle of $0.°5$ clockwise to correct for a systematic angular shift (Kuerster 1993), we find good position coincidences (within a few arcsec) between X-ray sources and optical objects from the APM catalog (e.g., http://www.ast.cam.ac.uk~lpinfo/apmcat/). Also, the centroid of the only point-like X-ray source in the field of the R-band image (Fig. 3; see also Lavery & Henry 1994) coincides with a star-like optical object. The source positions of the two X-ray observations are also in good agreement. The source-excised image is shown in Fig. 3; the residual source contamination in the image is negligible in comparison to the statistical counting uncertainty.

We select data to maximize the signal-to-background ratio of A2111. The integrated light curve of the RHRI observation shows time intervals of enhanced contaminations from scattered solar X-rays. We exclude all those intervals of contaminations greater than the cosmic X-ray background, resulting in an adopted effective exposure of 40,080 s. We include data in the RHRI pulse-height channels 1-7 only. These selections together reduce the non-cosmic X-ray background level in the data by $\sim 70\%$. The non-cosmic X-ray background contamination in the PSPC observation is mostly negligible (less than a few percent), and we obtain an effective exposure of 7288 s. However, due to the emission from the Galactic hot interstellar medium, the diffuse cosmic X-ray background is particularly bright in the soft band, defined here as the PSPC channel interval 20-41 (sensitive to photons primarily in the 0.14-0.28 keV range). Our imaging analysis is therefore chiefly in the hard band: 52-201 (0.5-2 keV). We further flat-field the images, using exposure maps constructed in individual bands (Snowden et al. 1994).

Our study of the galaxy distribution in A2111 is based on the R-band image (Figs. 4-5), a median of three 600s exposures taken on the UH 2.2 meter Mauna Kea telescope. Objects in the R-band image are morphologically classified with the Picture Processing Package (Yee 1991). The classification is complete down to 23.7 mag. Between this limit and 17 mag, we find a total 777 galaxy-like objects (Fig. 6).

3. Data Analyses and Results

Figs. 1-6 clearly show that A2111 has a complicated morphology. The cluster is strongly elongated at high X-ray intensity levels, and the degree of the elongation changes with intensity. The X-ray emission peak is off-set from the centroid of large-scale low surface brightness contours. The galaxy and X-ray distributions exhibit a similar elongation. No correlation between individual galaxies and X-ray emission enhancements can be discernible by eye, and an in-depth analysis is beyond the scope of this work. We now proceed to characterize both the spatial and spectral properties of the cluster and to examine its vicinity.

3.1. 1-D X-ray Surface Brightness Profiles

Although the morphology of A2111 clearly deviates from a circular symmetry, an 1-D characterization of the X-ray surface brightness distribution of the cluster can still be useful, especially for comparisons with observations of more distant clusters. To calculate such a profile we first obtain a local ML (maximum likelihood) centroid of the cluster X-ray emission peak within a $3'$ radius. We choose this radius to avoid complications caused by both the presence of discrete sources and nonuniform exposure of the observation at larger radii. The ML fit, similar to that described by Sarazin (1980), uses the standard β model of the form (Cavaliere & Fusco-Femiano 1976):

$$I = I_o \left(1 + \frac{r^2}{r_c^2}\right)^{1/2 - 3\beta}, \qquad (1)$$

where r is the off-centroid radius. We conduct the fit in an iterative fashion. In each iteration, we fix the centroid position and use only PSPC counts within the chosen radius. Because the radius is considerably small than the overall size of the cluster (e.g., Fig. 1), the fit does not provide tight constraints on the β model parameters (β, r_c, I_o, plus a uniform background). But the fit does determine the local centroid relatively well. The best-fit position is at $15^h 39^m 40\overset{s}{.}9, +34^d 25' 4''$ (R.A., Decl; J2000), and the 90% uncertainty is about $6''$.

Around the X-ray centroid, we calculate both the PSPC and RHRI surface brightness profiles, using source-removed count and exposure images. Fig. 7 and Table 1 show the results of β model fits to the profiles. The model parameters obtained from the two profiles are consistent with each other. Evidently, the β model provides a reasonably good description of the 1-D profiles. In particular, the profiles exhibit no enhanced central emission (above the β model), therefore no sign of a cooling flow in A2111. The 1-D characterization, however, is not sensitive to the 2-D substructure, which is apparent in the X-ray images.

3.2. 2-D Morphology

We characterize the 2-D diffuse X-ray morphology of A2111 with a series of ellipses on various scales (Fig. 8). Each ellipse is determined by four parameters: the center coordinates, ellipticity (ϵ), and orientation of the major axis (θ; north to east). We employ a simple moment method to calculate the parameters. This method was devised by Carter & Metcalfe (1980) to study the galaxy distribution of clusters. McMillan, Kowalski, & Ulmer (1989) and Buote & Canizares (1994) applied the method to X-ray images of nearby clusters. We compute the required first and second order moments, using positions of individual counts without binning, thus utilizing the full resolution of the data. Also because the detected number of counts per resolution element is much smaller than one (e.g., Fig. 3), the computation based on individual counts are more efficient than on image pixels.

Our computation follows an iterative procedure (see also Carter & Metcalfe 1980; Buote &

Canizares 1994). Starting with a circular region, we calculate the moments. We then derive the center coordinates, ellipticity, and orientation from the moments. These parameters, together with the semi-major axis, define an elliptical region. So we can return to calculate the moments and repeat the process until the changes in the computed parameter values all become less than 10^{-3}.

In each iteration, we explicitly subtract the expected background contributions to the moments. The computation of these background contributions is analogous to the calculation of the 2-D moments of inertia within an elliptical region of a uniform mass distribution. We estimate the background in a source-subtracted region between $10'$-$16'$ off-cluster, where cluster contribution is negligible. Small uncertainties ($\lesssim 10\%$) in the background estimate may change the derived parameters by a few percent, well within statistical errors.

Proceeding from a large radius to small ones, we obtained the parameters of the ellipses with their semi-major axes from $1'$ to $8'$. The parameters on different scales are not totally independent, because the computation uses the *aggregate* count distributions; on each scale, the parameters are average values within an ellipse, though weighted heavily by the outer parts of the region.

We estimate the uncertainties in the parameters, using a bootstrap algorithm. First, we generate 1000 bootstrap realizations by randomly re-sampling among count positions with replacement (e.g., Efron & Tibshirani 1993). Second, we apply the above moment method to each realization to obtain bootstrap replications of the ellipse parameters. Third, we sort the replications according to their values and use the 5% and 95% percentiles of the values as estimates of the 90% confidence interval of each parameter at a given semi-major axis.

Fig. 9 summarizes the results. The centroid coordinates of the cluster clearly shift with semi-major axis, caused primarily by the off-center emission peak. The global centroid, moment-weighted within the largest ellipse, is $\sim 13''$ northwest of the northern most of the two major galaxies. This galaxy (BOW # 6), at $\approx 15^h39^m40\overset{s}{.}4, +34^d25'27''$, has long been identified in the literature as the optical center of the cluster (Sandage, Kristian & Westphal 1976). The ellipticity also changes significantly (by a factor of ~ 2). The cluster is strongly elongated at a radius $\lesssim 6'$ and becomes more circular on larger scales. The variation in the position angle, though significant, is $\lesssim 20°$. These variations are, however, only a conservative characterization of the true morphological distortion of the cluster, because the parameters on different scales are correlated.

A similar analysis with the RHRI data at radii $\lesssim 4'$, where the signal-to-background ratio is relatively high, gives results that are statistically consistent with those from the PSPC data.

The galaxy distribution also shows an elongated morphology (Fig. 6). The distribution, characterized with an ellipse of a semi-major axis $3'$, has the centroid, ellipticity, and orientation as $15^h39^m40\overset{s}{.}6(-25'', +31''), +34°25'27''(-50'', +30''), 0.65(0.24\text{-}0.78)$, and $151(120\text{-}165)$ deg. The uncertainties are all at the 90% confidence level. These parameters are consistent with those from the X-ray data. Furthermore, the orientation between the two central major galaxies (BOW #5 and #6; Fig. 6) coincides well with the elongation of both the galaxy and X-ray distributions.

The two galaxies are $45''$ apart ($\sim 220h_{50}^{-1}$ kpc in projection) and are nearly identical in color and magnitude.

3.3.   Morphological Decomposition

We approximate the X-ray emission of A2111 as a superposition of a "subcomponent" on a large-scale "main component". Assuming that the subcomponent is responsible for the off-center peak, we define the main component in the relatively feature-free northwestern half of the cluster between $-107°$ and $73°$ (north to east). We calculate the PSPC surface brightness profile of the main component as a function of $r^2 = (-x\sin\theta + y\cos\theta)^2 + (x\cos\theta + y\sin\theta)^2/(1-\epsilon)^2$, expressed in the image coordinates (x, y) relative to the global centroid of the cluster. The coordinates of the centroid $(15^h39^m39\overset{s}{.}9, +34^d25'39'')$ as well as ϵ (0.17) and θ (167°) are from the ellipse fit with the semi-major axis equal to $8'$ (Fig. 9). We fit the profile using the β model as in Eq. (1), except that r_c is now the semi-major axis of the core. The best-fit is presented in Fig. 10, and the model parameters are $\beta = 0.65(0.54 - 0.84)$, $r_c = 0.56(0.39 - 0.82)$ Mpc, and $I_o = 9.5(7.7 - 11) \times 10^{-3}$ counts s^{-1} arcmin^{-2}. We then subtract this elliptical β model, extended two-dimensionally to the whole region in Fig. 3, from the surface brightness distribution of A2111.

The residual map in Fig. 11 demonstrates that the subcomponent is apparently a coherent structure. There are three distinct features: 1) a dominant blob centered between the two major galaxies; 2) a long, possibly twisted tail to the northwest; 3) a lobe to the southeast. Integrated over the region enclosed by the contour of 3×10^{-4} counts s^{-1} arcmin^{-2}, the total count rate of the subcomponent is ~ 0.056 counts s^{-1}, corresponding to an absorption-corrected luminosity of $\sim 2 \times 10^{44}h_{50}^{-2}$ ergs s^{-1} in the 0.1-2 keV band (§3.4). About 60% of this luminosity arises in the blob of $\sim 3'$ diameter. The over-subtraction in regions near the blob (Fig. 11) is, at least partly, due to the presence of the subcomponent tail. As the main component is a fit to the data that includes the tail, excluding the tail contribution from the fit would lead to an even flatter main component, and would, in turn, make the subcomponent even more prominent.

The above choice of the global moment-weighted X-ray centroid as the center of the main component is logical, but not unique. Alternatively, we may choose the central galaxy, which is about $13''$ southeast. This choice produces no qualitative change ($\lesssim 10\%$) in the 1-D profile of the main component, and slightly enhances the presence of the subcomponent tail. We conclude that the very presence and morphology of the subcomponent are due to both the ellipticity variation at different intensity levels and the off-center morphology of the cluster.

3.4.   X-ray Spectral Characterization

The limited spectral resolution and coverage of the PSPC data allow only a crude X-ray spectral characterization of A2111. We collected an on-cluster spectrum in a circle of $5'$ radius

around the cluster's local ML centroid (§3.1), and a background spectrum in a concentric annulus between $10'$ and $16'$ radii. The cluster contribution to the background in this annulus is negligible; different choices of the radii within the range between $8'$ and $18'$ results in no discernible change in the spectrum. The spectra are binned into the standard SASS channels (Snowden et al. 1994). We analyzed the spectra with the XSPEC package (e.g., http://heasarc.gsfc.nasa.gov/docs/xanadu/), assuming the Raymond & Smith thermal plasma model for the ICM emission. The spectra place only a 95%-confidence lower limit on the metal abundance of the ICM as $\gtrsim 22\%$ solar. We thus fixed the abundance to be 30% solar. Because the X-ray emission is dominated by thermal bremsstrahlung, the uncertainty in the abundance (within a factor of ~ 2; Mushotzky et al. 1996 and references therein) has little effect on the model fits (a few percent changes in the best-fit parameters). We further fix the abundance in X-ray-absorbing gas to be solar.

The best fit with $\chi^2/d.o.f = 28.6/28$ is satisfactory (Fig. 12). The measured temperature and absorbing-gas column density are 3.1(2.1-5.3) keV and $2.2(1.8 - 2.6) \times 10^{20}$ cm^{-2}; the parameter intervals are all at the 90% confidence. The column density agrees well with the Galactic atomic hydrogen column density of 1.9×10^{20} cm^{-2} from a 21 cm survey (Stark et al. 1992). With the best-fit parameters, we can convert the net cluster count rate 0.215 ± 0.007 counts s^{-1} within the $5'$ radius into an unabsorbed luminosity of $8.5 \times 10^{44} h_{50}^{-2}$ ergs s^{-1} in the cluster's rest-frame energy range 0.1-2 keV, or into a bolometric luminosity of $1.3 \times 10^{45} h_{50}^{-2}$ ergs s^{-1}. The uncertainty is about 20% in the 0.1-2 keV luminosity and is up to about 40% in the bolometric luminosity, within the quoted 90% limits of the spectral parameters. Similarly, we obtain an unabsorbed 0.1-2 keV flux/count-rate conversion of $5 \times$ and 1.5×10^{-11} ergs s^{-1} cm^{-2}/(counts s^{-1}) for the RHRI and the PSPC hard band, respectively. The flux is again calculated in the cluster's rest-frame 0.1-2 keV.

To find out whether or not the subcomponent is spectrally different from the rest of the cluster, we further split the above on-cluster spectrum into two: one from the dominant subcomponent region of $1'.2$ radius around the local ML centroid (§3.1), and the main component from the rest of the cluster. The radius is chosen so that the two spectra have approximately the same signal-to-noise ratios. The contamination between the two components tends to reduce the actual spectral difference.

We fit the spectra jointly. Assuming that the absorptions in the two regions are the same, we obtain the sub- and main-component temperatures (keV) as 4.4 (2.2-15) and 2.7 (1.8-4.5). This temperature difference becomes a little more significant (at $\sim 95\%$ confidence), if we fix the absorption to the 21 cm measured Galactic value. Therefore, the average temperature of the ICM in the subcomponent appears higher than in the rest of the cluster.

3.5.   Vicinity of A2111

The combination of the PSPC and RHRI observations allows us to detect extended sources as candidates for additional clusters in the vicinity of A2111. It turns out that the brightest PSPC source ($15^h39^m1^s\!.2, +34°36'8''$), besides A2111, in our examined region (Fig. 1) is such a candidate. The source is extended at the confidence level of 99.7%, has a count rate of $7.6 \pm 1.2 \times 10^{-3}$ counts s^{-1}, and has a hard spectrum consistent with a thermal plasma of several keV. The source can be barely seen as an extended feature in the RHRI image (Fig. 2). This weak contrast of the source is due to both the high non-cosmic X-ray background and the degraded RHRI PSF near the edge of the image. The integrated flux within a $30''$ radius is consistent with that inferred from the PSPC rate.

Furthermore, the X-ray source is apparently associated with a compact group of optical objects (Fig. 2), which are classified as either galaxies or multiple objects in the APM catalog. The source is thus likely a cluster (the NW cluster hereafter). Three major optical objects in the group appear a bit brighter than galaxies in A2111, indicating that the group is probably not as distant as A2111. However, if this cluster is at the same redshift as A2111, the implied 0.1-2 keV luminosity is then $\sim 3 \times 10^{43} h_{50}^{-2}$ ergs s^{-1} (or about 4% of the A2111's), reasonable for the apparent optical richness. Incidentally, the cluster is projected in a position to which A2111 directs its subcomponent's tail.

4.   Discussion

4.1.   General Consideration

Can A2111 be a chance superposition of two noninteracting clusters? To produce the observed off-center morphology, A2111 needs a superimposed cluster that is 2-3 times brighter than that of the NW cluster. The statistical probability for such a superposition is small ($\sim 10^{-2}$). Furthermore, if the superimposed cluster has an approximately circular or elliptical morphology, we would still have difficulties in reproducing the tail of the subcomponent. In addition, based on the redshift measurements of 24 objects in the A2111 field, Lavery & Henry (1986) find no strong evidence for a superposition of a foreground or background cluster with A2111. Six field galaxies were identified at five distinct redshifts. Therefore, the subcomponent is most likely intrinsic to A2111.

4.2.   A2111 as a Head-on Subcluster Collision

Our results have strong implications on the dynamic state of A2111. First, as argued by Mohr, Fabricant, & Geller (1993), the shift of X-ray image centroid indicates that the center of mass of the cluster is changing as a function of scale and that the cluster is not a relaxed,

equilibrium system (see also Ulmer, McMillan, & Kowalski 1989). Second, our identification of the comet-shaped subcomponent suggests that this unstable state is most likely the result of a major subcluster merger. Third, the approximate alignment among the subcomponent elongation, the galaxy distribution, and the relative orientation of the two major galaxies indicates that the merger is a nearly head-on collision. The closeness of the two major galaxies, which may well be the central galaxies of the two merging components, is consistent with a recent core impact.

By comparing our observed characteristics of A2111 with N-body/hydrodynamic simulations of such collisions (Schindler & Müller 1993; Roettiger, Burns, & Loken 1993; Pearce, Thomas, & Couchman 1994), we can learn more about the merger history and process. According to the simulations, the ICM can have been heated by the passage of the subcluster, consistent with the flat X-ray distribution of the main component in the northwestern part of A2111 (§3.3). A shock may have developed during the core impact. The present position of the shock front is presumably represented by the compression at the southeastern edge of the subcomponent blob and by the fan-shaped contours on both sides of the blob, indicating an invasion of the subcluster from the northwest along the major axis.

This merger scenario also naturally explains the morphology and thermal state of the subcluster, as characterized by the subcomponent. The subcluster, forcing into the main cluster, should have left a trail of X-ray-emitting gas relics, which might be responsible for the subcomponent tail. The simulations show that the ICM inside the subcluster, emerging out from the core of the main cluster, should be heated to a temperature of $\sim 10^8$ K. Consistent with being so hot (§3.4), the blob of the subcomponent may represent the core of the subcluster. The ram-pressure confinement of the snow-plowing subcluster accounts for the high X-ray intensity of the blob.

The lobe in front of the blob is very intriguing, however. If the subcluster is now falling back to the main cluster center, the residual of the subcluster may then explain the lobe. But, totally absent in the PSPC soft band (Fig. 5), the lobe probably has a hard spectrum, inconsistent with the prediction of a low temperature $\sim 5 \times 10^6$ K (e.g., Roettiger, Burns, & Loken 1993). Alternatively, the feature may represent a separate subcluster. Fig. 6 indeed shows a condensation of galaxies in the region. But the true nature of the feature remains uncertain.

The average ICM temperature of A2111, 3.1(2.1-5.3) keV (§3.4), is low, compared to clusters of comparable optical richness (e.g., Edge & Stewart 1991). The Coma cluster ($N_{30\%} = 94$; $f_b = 0.03 \pm 0.01$) is an example. The temperature 9.1 ± 0.7 keV of this nearby cluster (Hughes, Gorenstein, & Fabricant 1988) is about a factor of 2 higher than that of A2111. As a distant example, the well-known cluster CL0016+16 ($N_{30\%} = 65$; $f_b = 0.02 \pm 0.07$) at $z = 0.54$, has a temperature of 8.2(6.7 − 10) keV (Neumann & Böhringer 1996 and references therein).

The relatively low ICM temperature of A2111 may be directly related to the ongoing major merger. Individual components before the merger can be considerably cooler. Relatively cool gas originally on the outskirts of the components may have penetrated into the central region

of the current system, resulting in enhanced soft X-ray radiation. Furthermore, if A2111 is of multi-temperatures and if a pressure balance approximately holds, a cooler component tends to have a higher emission measure. The soft emission from this cooler component, dominating in the *ROSAT* band, could have resulted in an underestimate of the average ICM temperature. An upcoming *ASCA* observation will, we hope, provide more conclusive data on the multi-temperature state of the cluster.

Our data indicate an absence of a cooling flow in A2111. The head-on collision could have destroyed such a flow, if existing previously (Roettiger, Burns, & Loken 1993). Currently, the cooling time scale at the X-ray emission peak, for example, is $\sim (2 \times 10^{10} \text{ yr})h_{50}^{-1/2}(T_e/10^8 \text{ K})^{1/2}$, likely longer than the age of the cluster.

Strong evidence for major subcluster mergers has been observed in two nearby clusters: A2256 ($z = 0.060$; Briel et al. 1991; Briel & Henry 1994; Markevitch 1996) and A754 ($z = 0.054$; Henry & Briel 1995; Henriksen & Markevitch 1996). The overall X-ray morphology of A754 resembles that of A2111. But, the off-center emission peak in A754 appears as a bar nearly perpendicular to the overall elongation of the cluster, and has a temperature (~ 3 keV) lower than the cluster average (~ 9 keV). Henriksen & Markevitch (1996) show that the X-ray surface brightness and temperature distributions of A754 are consistent with a non-head-on merger (e.g., Evrard, Metzler, & Navarro, 1996). This scenario may also explain the large separation, $12'$ (a projected distance of ~ 1 Mpc; Henry & Briel 1995), between the two major galaxies in the cluster. A similar interpretation may also hold for A2256. The subcomponent of A2256 is cooler (~ 4 keV) than the surrounding medium (~ 8 keV), and has a distinct compression of contour lines in the direction approximately perpendicular to the major axis of the cluster. This compression is presumably due to the snowplow effect on the leading edge of the subcluster (Briel et al. 1991), indicating that the subcluster is *spiraling* into A2256. Therefore, the impact appears to be a non-head-on collision as well. In comparison, the orientation of the subcomponent in A2111 is nearly parallel, instead of perpendicular, to the major axis of the cluster in both X-ray and optical, and the gas temperature of the subcomponent appears hotter, instead of cooler, than the cluster average.

4.3. The Subcluster Merger and the Blue Galaxy Population

A2111 contains a high fraction ($f_b = 0.16 \pm 0.03$) of blue galaxies, as measured both photometrically (BO) and spectroscopically (Lavery & Henry 1986). Lavery & Henry (1988, 1994) further show that the large majority of the blue galaxies in A2111 have disk-like morphology and that star formation is extended over galactic disks in two nearly face-on spiral galaxies. Could the ongoing merger be responsible?

An ongoing merger is expected to contain a larger fraction of spiral galaxies than a relaxed cluster of the same mass. Generally, the spiral fraction f_{sp} of a cluster is known to decrease with increasing X-ray luminosity (or the richness; Bahcall, 1977); for nearby clusters, most of which are

more-or-less relaxed systems, $f_{sp} \approx 10^{15} L_{bol}^{-0.35}$ and $L_{bol} \propto \sigma^{2.90}$, where σ is the galaxy velocity dispersion (Edge & Stewart 1991). Because the number of galaxies in a relaxed cluster $N_g \propto \sigma^2$, we have $f_{sp} \propto N_g^{-0.51}$. Thus, an average nearby cluster with an X-ray luminosity of A2111's (§3.4) is expected to have $f_{sp} \sim 0.16$. For a cluster at the redshift of A2111, we assume a more general form $f_{sp} \propto N_g^{-\gamma}$, where f_{sp} may also include late-type galaxies besides spirals. Simple algebra shows that a merger of two relaxed subclusters results in a system of an initial spiral fraction $f_{sp}^m \approx f_{sp}(1 + r_g^{1-\gamma})/(1 + r_g)^{1-\gamma}$, where r_g is the galaxy number ratio of the subclusters. When the two subclusters have the equal number of galaxies (i.e., $r_g = 1$), $f_{sp}^m = 2^\gamma f_{sp}$, which is the maximum if $\gamma < 1$ (or the minimum if $\gamma > 1$). If $\gamma \sim 0.51$, for example, the f_{sp}^m value of A2111 is then about 0.23. This spiral fraction can be substantially larger, if γ is greater and/or if the merger involves more than two subclusters. However, no all spirals are blue galaxies as defined by BO.

The merger may further trigger starbursts in some of the spirals, accounting for the large fraction of blue galaxies observed in A2111. The starbursts could result from an enhancement of two-body interactions in the infalling subcluster (Lavery & Henry 1988: Lavery, Pierce, & McClure 1992), from frequent encounters with cluster members, together with the tidal forces of the mean cluster potential (Moore et al. 1996; Henriksen & Byrd 1996), and/or from the high pressure of the ICM. The blue galaxies of A2111 show a higher velocity dispersion, by about 50%, than the red cluster members (Lavery 1988), consistent with the ongoing merger scenario. The cluster environmental effects can also gradually transform late-type galaxies to early-type ones (Oemler et al. 1997), resulting in the decrease of the spiral fraction with time after a merger.

In an ongoing study of other distant ($z \gtrsim 0.2$) BO clusters observed with the *ROSAT* PSPC (Wang & Ulmer 1997 in preparation), we find that clusters of high f_b consistently show relatively low average ICM temperatures, contain substantial amounts of substructure, and tend to be strongly elongated. Thus a high f_b value of a cluster is an indicator of a dynamically young system. Furthermore, according to the hierarchical clustering theories of the structure formation, an observed high-z rich cluster is typically a younger system and is assembled from units of smaller masses than a present-day cluster of the same mass. Therefore, the increasing f_b of rich clusters with z — the Butcher & Oemler effect — is a natural consequence of the hierarchical structure formation process (Kauffmann 1995).

5. Summary

Based on our *ROSAT* PSPC and RHRI observations, plus a deep R-band CCD image, we have conducted a detailed spatial and spectral analysis of the richest BO cluster A2111. Our analysis includes a 2-D morphological characterization of the cluster, using a moment method improved to remove background effects. We find that the cluster has a strongly elongated morphology, similar in optical and X-ray, and that both the centroid and ellipticity of the X-ray morphology vary significantly with scale.

We conclude that A2111 contains at least two major X-ray-emitting components. The main component, characterized by the northwestern half of the cluster's X-ray emission, has a flat distribution, whereas the subcomponent is more-or-less comet-shaped. The orientation of the subcomponent aligns well with the elongation of both the galaxy and the X-ray surface brightness distributions of the cluster. The gas in the subcomponent appears hotter than in the main component. The average ICM temperature of A2111 is, however, unusually low (by a factor of ~ 2), compared to clusters of similar optical richness.

The characteristics of the subcomponent suggest that A2111 represents a head-on merger between two clusters. Numerical simulations of such mergers show similar morphological and spectral features as observed in A2111, if the core impact has just occurred. This ongoing merger is also likely responsible for the high blue galaxy fraction of the cluster.

Table 1
β Model Characterization of the X-ray Surface Brightness Profiles[a]

Parameter	PSPC	RHRI
β	0.54 (0.50-0.59)	0.47 (0.44-0.52)
r_c (h_{50}^{-1} Mpc)	0.21(0.17 - 0.26)	0.18(0.15 - 0.22)
I_o(10^{-2} cts s^{-1} arcmin^{-2})	3.2(2.7-3.8)	1.5(1.3-1.7)
$n_{e,o}$($10^{-3}h_{50}^{1/2}$ cm^{-3})	3.9 (3.4-4.6)	4.1 (3.6-4.7)
$\chi^2/d.o.f$	47.8/36	72.5/68

[a]Uncertainties in parameter values, as presented in parentheses, are all at the 90% confidence level. The derivation of the central electron number density $n_{e,o}$ assumes an oblate shape of the X-ray-emitting medium and the best-fit Raymond & Smith model of the integrated PSPC spectrum of A2111 (§3.4).

REFERENCES

Briel, U. G., & Henry, J. P. 1994, Nature, 372, 439

Briel, U. G., et al. 1991, A&A, 246, L10

Buote, D. A., & Canizares, C. R. 1994, ApJ, 427, 86

Butcher, H., Oemler, A., & Wells, D. C. 1983, ApJS, 52, 183

Butcher, H., & Oemler, A. 1984, ApJ, 285, 426 (BO)

Carter, D., & Metcalfe, N. 1980, MNRAS, 191, 325

Cavaliere, A., & Fusco-Femiano, R. 1976, A&A, 49, 137

Couch, W. J., Ellis, R. S., Sharples, R. M., & Smail, I. 1994, ApJ, 430, 121

Dressler, A., & Shectman, S. A. 1988, AJ, 95, p85

Dressler, A., & Gunn, J. E. 1992, ApJS, 78, 1

Edge, A. C., & Stewart, G. C. 1991, MNRAS, 252, 414

Efron, B., & Tibshirani, B. J. 1993, in An Introduction to the Bootstrap, Champman & Hall, New York

Evrard, A. E., Metzler, C. A., & Navarro, J. F. 1996, ApJ, 469, 494

Fabricant, D. F., Bautz, M. W., & McClintock, J. E. 1994, AJ, 107, 8

Geller, M. J., & Beers, T. C. 1982, PASP, 94, 421

Hasinger, G., et al. 1994, Legacy, 4, 40

Henry, J. P., & Briel, U. G. 1995, ApJL, 443, 9

Henriksen, M. J., & Byrd, G. 1996, ApJ, 459, 82

Henriksen, M. J., & Markevitch, M. L. 1996, ApJL, 466, 79

Hughes, J. P., Gorenstein, P. D., & Fabricant, D. 1988, ApJ, 329, 82

Jones, C., & Forman, W. 1992, in Clusters and Superclusters of Galaxies, ed. A. C. Fabian (Dordrecht: Kluwer), 49

Kauffmann, G. 1995, MNRAS, 274, 161

Kuerster, M. 1993, ROSAT Status Report, No. 67

Lavery, R. J. 1988, PhD. thesis, University of Hawaii

Lavery, R. J., & Henry, J. P. 1986, ApJL, 304, 5

Lavery, R. J., & Henry, J. P. 1988, ApJ, 330, 608

Lavery, R. J., & Henry, J. P. 1994, ApJ, 426, 524

Lavery, R. J., Pierce, M. J., & McClure, R. D. 1992, AJ, 104, 2067

Markevitch, M. 1996, ApJL, 465, 1

McMillan, S. L. W., Kowalski, M. P., & Ulmer, M. P. 1989, ApJS, 70, 723

Mohr, J. J., Fabricant, D. G., & Geller, M. J. 1993, ApJ, 413, 492

Mushotzky, R. F., et al. 1996, ApJ, 466, 686

Neumann, D. M., & Böhringer, H. 1996, preprint astro-ph/9607063

Newberry, M. V., Kirshner, R. P., & Boroson, T. A. 1988, ApJ, 335, 629

Nichol, R., Ulmer, M. P., Kron, R. G., Wirth, G. D. & Koo, D. C. 1994, ApJ, 432, 464

Bahcall, N. A. 1977, ApJL, 218, 93

Oemler, A., Dressler, A., & Butcher, H. R. 1997, ApJ, 474, 561

Pearce, F. R., Thomas, P. A., & Couchman, H. M. P. 1994, MNRAS, 268, 953

Roettiger, K., Burns, J., & Loken, C. 1993, ApJ, 403, L53

Sandage, A., Kristian, J., & Westphal, J. A. 1976, ApJ, 205, 688

Sarazin, C. L. 1980, ApJ, 236, 75

Schindler, S., & Müller, E. 1993, A&A, 272, 137

Snowden, S. L., McCammon, D., Burrows, D. N., & Mendenhall, J. A. 1994, ApJ, 424, 714

Stark, A. A., et al. 1992, ApJS, 79, 77

Tomita, A. et al. 1996, AJ, 111, 42

Trümper, J. 1992, QJRAS, 33, 165

Ulmer, M. P., McMillan, S. L. W., & Kowalski, M. P. 1989, ApJ, 338, 711

Yee, H. K. C. 1991, PASP, 103, 396

Zabludoff, A. I., et al. 1996, ApJ, 466, 104

Fig. 1.— PSPC image of A2111 in the 0.5-2 keV band. The contours represent the distribution of the X-ray surface brightness, which has been corrected for exposure and has been smoothed adaptively with a Gaussian, the size of which is adjusted at each pixel to achieve a count-to-noise ratio of 4. Each contour is 2σ (50%) above its lower level; the lowest contour is at 3.4×10^{-4} counts s^{-1} arcmin^{-2}.

Fig. 2.— RHRI surface brightness contours overlaid on the digitized optical sky survey image of the A2111 field. The X-ray surface brightness distribution has been smoothed with a Gaussian of size $30''$ (FWHM), comparable to the RHRI PSF at corners of the field. The contours are at 1.4, 2.0, 2.6, 3.2, 3.8, 5.0, 6.2, 7.4, 8.6, 9.8, 11, and 12 $\times 10^{-3}$ counts s^{-1} arcmin^{-2}. *Crosses* mark point-like X-ray sources detected outside the central $3'.5$ radius.

Fig. 3.— PSPC image of A2111 in the 0.5-2 keV band after point-like X-ray sources are excised. Individual dots represent PSPC counts in the 0.5-2 keV band. The regions within 90% source flux-encircled radii are replaced by randomly generated counts with intensity interpolated from neighboring average. The rest is the same as in Fig. 1.

Fig. 4.— RHRI intensity contours overlaid on the R-band image of A2111. The X-ray surface brightness is adaptively smoothed to achieve a count-to-noise ratio of ~ 6 over the image. The contours are at 1.2, 2.1, 3.2, 4.8, 6.9, 9.7, 13, 18, and 25×10^{-3} counts s^{-1} arcmin^{-2}.

Fig. 5.— PSPC surface brightness contours in the 0.14-0.28 keV band (upper panel) and in the 0.5-2 keV band (lower panel) superposed on the R-band CCD image of A2111. The soft band contours are at 0.75, 1.1, 1.7, 2.5, and 3.8 10^{-3} counts s^{-1} arcmin^{-2}. The rest is the same as in Fig. 1.

Fig. 6.— Distribution of galaxies in the central field of A2111. The galaxies, represented by *pluses*, are selected in the magnitude range of 17 to 23.7. The contours illustrate the distribution after being adaptively smoothed with a Gaussian filter of a count-to-noise ratio ~ 4, and are at 12, 18, and 27 galaxies arcmin^{-2}. Two main galaxies in the central region are marked as *diamonds*.

Fig. 7.— Radial surface brightness profiles of A2111 derived from the PSPC observation (a) and the RHRI observation (b). The data are represented by *crosses* with standard error bars. The curves represent the best fits of the β model to the profiles.

Fig. 8.— Characterization of the 2-D X-ray morphology of A2111 with ellipses on scales from $1'$-$8'$. The triangle marks the global X-ray centroid determined on the largest scale. The dots represent PSPC counts as in Fig. 3.

Fig. 9.— Center coordinates, ellipticity, and orientation of the ellipse as a function of semi-major axis. The coordinates are relative to the central galaxy position $15^h39^m40\overset{s}{.}4, +34^d25'27''$. Error bars are at the 90% confidence level. Note that individual measurements are not statistically independent (see text).
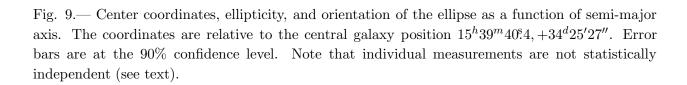
Fig. 10.— PSPC surface brightness profile as a function of the semi-major axis in the main-component elliptical coordinates (see text). The rest is the same as in Fig. 7.

Fig. 11.— PSPC surface brightness residuals, after subtracting the elliptical β model from Fig. 6. The contours are at -1.2, -0.6, -0.3, 0.3, 0.6, 1.2, 2.4, 4.8, 9.6, and 19.2 $\times 10^{-3}$ counts s^{-1} arcmin^{-2}. The two main galaxies are marked as diamonds. The ellipse illustrates the ellipticity and orientation of the main component.

Fig. 12.— PSPC spectrum of A2111 and the best-fit Raymond & Smith model (histogram).

This figure "f1.gif" is available in "gif" format from:

http://arXiv.org/ps/astro-ph/9702035v1

This figure "f2.jpg" is available in "jpg" format from:

http://arXiv.org/ps/astro-ph/9702035v1

This figure "f3.gif" is available in "gif" format from:

http://arXiv.org/ps/astro-ph/9702035v1

This figure "f4.jpg" is available in "jpg" format from:

http://arXiv.org/ps/astro-ph/9702035v1

This figure "f5.jpg" is available in "jpg" format from:

http://arXiv.org/ps/astro-ph/9702035v1

This figure "f6.gif" is available in "gif" format from:

http://arXiv.org/ps/astro-ph/9702035v1

This figure "f7a.gif" is available in "gif" format from:

http://arXiv.org/ps/astro-ph/9702035v1

This figure "f7b.gif" is available in "gif" format from:

http://arXiv.org/ps/astro-ph/9702035v1

This figure "f8.gif" is available in "gif" format from:

http://arXiv.org/ps/astro-ph/9702035v1

This figure "f9.gif" is available in "gif" format from:

http://arXiv.org/ps/astro-ph/9702035v1

This figure "f10.gif" is available in "gif" format from:

http://arXiv.org/ps/astro-ph/9702035v1

This figure "f11.gif" is available in "gif" format from:

http://arXiv.org/ps/astro-ph/9702035v1

This figure "f12.gif" is available in "gif" format from:

http://arXiv.org/ps/astro-ph/9702035v1